ACCSCIENCE PUBLISHING

Materials Science in Additive Manufacturing

ORIGINAL RESEARCH ARTICLE

Strategies for high-quality fabrication of Inconel 625 parts via powder bed fusion–laser beam

Mohsen Afshani[1]*, Mariangela Quarto[1]*, Sara Bocchi[1], Gabriele Locatelli[1], Tommaso Persico[2], and Gianluca D'Urso[1]

[1]Department of Management, Information and Production Engineering, University of Bergamo, Dalmine, Bergamo, Italy

[2]Department of Engineering and Applied Sciences, University of Bergamo, Dalmine, Bergamo, Italy

Abstract

Additive manufacturing, particularly powder bed fusion–laser beam (PBF–LB) technology, offers new opportunities for fabricating complex alloy components with enhanced design flexibility. Specifically, Inconel 625 (IN625), a nickel-based superalloy, is widely used in high-performance applications because of its excellent mechanical properties and corrosion resistance. However, the quality of PBF–LB-manufactured parts is highly sensitive to process parameters, especially the volumetric energy density (VED). This study investigated the effects of laser power (*P*) and scan speed (*v*) on the quality of IN625 samples produced via PBF–LB. A total of 60 samples were fabricated across three build plate rotation angles (0°, 90°, and 180°) and evaluated for porosity, surface morphology, and microhardness, revealing a clear correlation between VED and key quality metrics. Optimal material properties were achieved within a VED range of 66–100 J/mm^3, whereas deviations from this range led to defects such as a lack-of-fusion, keyholing, and balling. Additionally, maintaining a balanced relationship between *P* and *v* while keeping the other parameters constant was found to be essential for proper melting and defect mitigation. The results further indicate that, under the tested conditions, the rotation of the build plate and the position of the specimen have no significant influence on the quality or properties of the part. Overall, the findings highlight the critical role of process parameter control in producing dense, defect-minimized IN625 parts via PBF–LB.

Keywords: Inconel 625; Additive manufacturing; Powder bed fusion–laser beam; Process parameters; Volumetric energy density; Process optimization

***Corresponding authors:**
Mohsen Afshani
(mohsen.afshani@unibg.it)
Mariangela Quarto
(mariangela.quarto@unibg.it)

Citation: Afshani M, Quarto M, Bocchi S, Locatelli G, Persico T, D'Urso G. Strategies for high-quality fabrication of Inconel 625 parts via powder bed fusion–laser beam. *Mater Sci Add Manuf*. doi: 10.36922/MSAM026130022

Received: March 29, 2026

Revised: April 23, 2026

Accepted: May 7, 2026

Published online: June 3, 2026

1. Introduction

Additive manufacturing (AM) is an advanced manufacturing technology developed over the past 30 years and encompasses a set of techniques that produce three-dimensional (3D) components from virtual models generated by computer-aided design software.[1-4] These technologies allow the production of complex 3D components of any shape by utilizing 3D model data that are impossible to fabricate through traditional manufacturing techniques. Among all available technologies, laser powder bed fusion (PBF–LB) is one of the most promising AM technologies for metals, which uses a laser beam with adequate energy to melt pre-laid thin metal powder layer by layer (generally

between 20 and 100 μm) and form high-performance parts after cooling and solidification.[5-7] Several AM techniques are focused on the production of complex geometries and structure components, such as stereolithography, digital light processing, selective laser sintering, direct metal laser sintering, electron beam melting, fused deposition modeling, multijet/polyjet 3D printing, selective laser melting, and laminated object manufacturing.[4,8] Among all these technologies, PBF–LB can be used to produce parts from both pure and alloyed metal powders. Volumetric energy density (VED) is often used as a predictor for part relative density in PBF–LB processes. Various formulations of this parameter exist. VED is typically defined as the ratio of laser power (P) to the product of scan speed (v), hatch spacing (h), and powder bed layer thickness (t) (Figure 1). It represents the amount of energy delivered per unit volume of powder in the bed, directly influencing key dimensions, particularly the penetration depth.[9,10] It is worth noting that in some literature, the laser beam diameter is used instead of hatch spacing to calculate the energy density,[11] but in the present study, a more common formula was adopted to examine the parameters (**Equation 1**). PBF–LB is especially suitable for forming small batches, high-value, customized, and complex structural parts for aerospace, biomedical, automotive, abrasive, and other applications.[12-15]

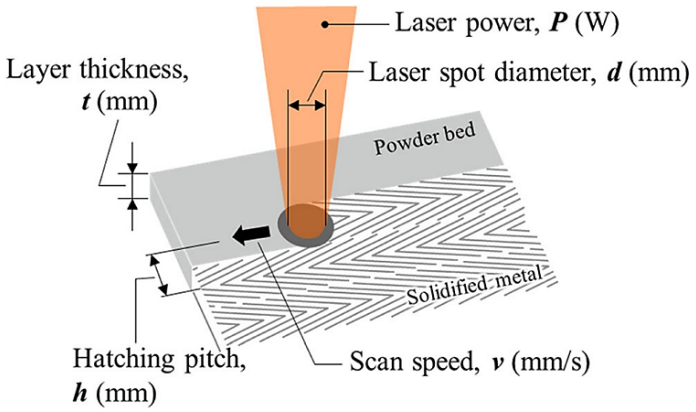

Figure 1. Schematic of the powder bed fusion–laser beam process and various parameters used to determine the volumetric energy density formulation. Reprinted with permission from Yonehara *et al.*[16] Copyright © 2020, Springer-Verlag London Ltd., part of Springer Nature.

$$VED = \frac{P}{v.h.t}\left[\frac{J}{mm^3}\right] \quad (1)$$

Inconel 625 (IN625) is a nickel–chromium–molybdenum solid-solution-hardened wrought superalloy that presents a combination of high-temperature strength and very high corrosion and oxidation resistance, even at temperatures up to approximately 1,000 °C.17-19 Table 1 shows its nominal chemical composition.

At the current state-of-the-art, the established and commercialized process parameters for PBF–LB allow the production of defect-free components of IN625 with a density close to 100%, due to its high weldability.[20-22] There is also growing interest in the mechanical properties required for structural materials, particularly their fatigue and creep resistance.[23,24] Koutiri *et al.*[25] studied the fatigue behavior of as-built IN625 produced via PBF–LB, focusing on the effects of surface finish conditions and porosity (including pore location). The results were consistent with expectations: PBF–LB-manufactured IN625 with high surface roughness (Ra) and numerous defects, such as pores and lack-of-fusion (LOF), exhibited a significantly reduced fatigue life. To address this issue, Marchese *et al.*[26] mentioned that it is crucial to perform post-heat treatments to reduce defects such as residual stresses, develop the desired microstructure and texture, and achieve mechanical properties that meet or exceed those of post-heat-treated IN625 alloy in its traditional state. In addition, during melting and solidification, which are governed by a complex thermal cycle, heat flux dissipation from the top of the samples to the building platform promotes the formation of columnar grains, leading to anisotropic mechanical properties. Consequently, the orientations of the components on the building platform must be carefully considered.

In the PBF–LB process, defects such as pores, inclusions, cracks, LOF, keyholing, balling, and poor interlayer fusion may also be induced during printing due to improper control of the forming process, thereby further affecting the mechanical properties of the fabricated parts. Metallurgical defects of IN625 obtained by the PBF–LB process are summarized in Table 2.

Table 1. Nominal compositions of Inconel 625[17]

Element	Nickel	Chromium	Molybdenum	Titanium	Niobium	Iron	Aluminum	Carbon
Composition (wt.%)	58 (minimum)	20–23	8–10	0.4	3.15–4.15	5	0.2–0.4	0.05

Table 2. Main defects and reasons for the formation of powder bed fusion–laser beam Inconel 625 alloy parts

Density	Defects	Formation reasons	Elimination (Weakening) measures	Ref.
Almost 100%	A lack-of-fusion, gas entrapment, and porosity	Powder factor	Reasonable process parameters	27
	Macro defect: Balling, irregularity, distortion, spatter, unmelted particles, necking Micro defect: Unmelted, inclusions, cracks, porosity (20~100 μm)	Insufficient heat input, low melt viscosity, and instability of the melt pool	Reasonable process parameters	28
	Surface topography: Open pore, balling, microcracks Subsurface defect: Pores	Uneven layer thickness distribution, high tensile residual stress, high viscosity, and surface tension of the melt pool material	-	29
	Surface cracks, internal inclusions	Oxidation, residual thermal stress	Annealing	30
99%	Surface cracks	Local eutectic structure (γ + Laves), residual thermal stress	Substrate preheating	31
Related to laser parameters	Most pores and a small number of cracks in interlayer boundaries	-	-	32

Regarding these issues, Li *et al.*[29] mentioned that the apparent porosity and balling spheres are the main reasons for the poor surface finish of as-built IN625 alloy samples. When macroscopic defects occur in the PBF–LB sample, microscopic defects also increase. Generally, to set adequate energy, it is necessary to consider (i) an extremely low energy input results in insufficient melting or "LOF" porosity, whereas (ii) an extremely high energy input results in "keyholing."[33-35] Briefly, LOF, as the name suggests, is the result of incomplete welding of layers or adjacent melt pools, resulting in an irregular morphology,[36,37] and keyholing is a welding term for the deep, narrow vapor depression that forms under high-energy-density melting conditions due to metal vaporization beneath the heat source.[38] On the other hand, due to low v and high repetition rates, the balling phenomenon severely impedes interlayer bonding, reducing part density and increasing both top and side Ra. However, its effect is more pronounced on side roughness, as the scattered balls predominantly accumulate along the sides of the melt pool rather than on the top surface.

Nevertheless, in this study, the probabilities of the aforementioned defects (both predicted and real) across varying VED values and build plate rotations were analyzed. The predicted defects were identified on the basis of an extensive review of the literature,[39-42] whereas the real defects were directly observed on the fabricated samples. Unlike conventional works that focus either on single process parameters or limited VED ranges,[43,44] this work systematically correlates a wide range of VED values with both surface and volumetric defects while also investigating the influence of build plate rotation. This integrated approach provides new insights into optimizing process windows for IN625 fabrication via PBF–LB.

The aim of this study is to investigate how P and v (and consequently the VED) affect the manufacturing quality of IN625 specimens fabricated via PBF–LB. In the first stage, cylindrical specimens were fabricated using PBF–LB in three runs with different build plate rotations. In the second stage, the as-built samples were characterized by Ra measurement, Vickers microhardness (HV) testing

on both the top and bottom surfaces, and porosity analysis of the cross-sections perpendicular to the build direction. This work provides a unified experimental framework that simultaneously examines these characteristics across a wide VED spectrum. Despite its limited predictive capability due to the omission of how different parameter combinations affect melt pool physics,[11] VED remains a useful indicator for initial analysis and optimization. It also provides a convenient, common metric for comparing results across different studies, enabling the identification of general process trends and the formulation of preliminary processing guidelines.

A distinctive feature of this study lies in its incorporation of build plate rotation as a secondary factor to assess spatial consistency and potential thermal gradient effects. Furthermore, this work offers a critical validation of literature-based defect prediction thresholds through direct experimental observations. This systematic comparison between predicted and actual defect formation across different processing conditions has not been widely discussed in previous research. Despite the extensive literature on the PBF–LB process applied to IN625, several aspects remain unclear. In particular, previous research was focused on isolated process parameters or narrow processing windows, with limited integration of multiple quality indicators within a single experimental framework. In this context, the present work aims to address two main gaps: (i) define a systematic correlation of a wide range of VED values with both predicted defect regimes extrapolated from the literature and experimentally observed defects; and (ii) provide a combined and comparative analysis of Ra, porosity, and microhardness to identify the overall material response. The integrated approach enables a more comprehensive understanding of the process–structure–property relationships in PBF–LB of IN625 and provides practical insights for defining robust processing windows.

2. Materials and methods

2.1. Specimen fabrication

The IN625 powders used in this work were sieved, and the grain-size distribution was analyzed using a laser diffraction particle size analyzer, the Mastersizer 3000 (Malvern Panalytical, United Kingdom), with a particle size range of 21–48 μm.

As illustrated in Figure 2A, cylindrical specimens with a 10 mm diameter and a 6 mm thickness were produced using a laser powder bed fusion machine (Print Genius 150, Prima Additive s.r.l., Italy) with a circular build platform. *P* and *v* were varied at 5 and 4 levels, respectively. It should be noted that *h* and *t* were intentionally kept constant to isolate the effects of *P* and *v,* and consequently of VED, on the material response. This approach allows a more controlled investigation of the primary process parameters. Hatch spacing and layer thickness are known to affect melt pool overlap, thermal gradients, and defect formation, and their influence should be considered in future studies. A full factorial plan was considered for the sample production as reported in Table 3. Because of the variation in *P* and *v*, each sample had a different VED value. As shown in Figure 2B, each specimen was assigned an identification number from 1 to 20.

To evaluate the influence of printing position and gas flow, the build job was repeated three times, and the build plate was rotated 90° counter-clockwise around the build direction (Z-axis) from its original orientation, as illustrated in Figure 3. More specifically, in the first run, the samples were printed such that sample No. 1 was positioned in the far bottom-left corner, far from the gas inlet. In the second run, sample No. 16 occupied the bottom-left corner, while sample No. 1 was placed in the first row, closest to the gas inlet, and in the third run, sample No. 20 was positioned far from the gas inlet, directly opposite to its position in the first run. In total, 60 test samples were produced for analysis.

After specimen preparation, the build plate was carefully removed from the machine and cleaned using a specialized brush to remove any residual powder. Unfused powders were then carefully removed using a vacuum system. The samples were subsequently prepared for further experimental analysis.

2.2. Characterization

The as-built specimens were comprehensively characterized, focusing on surface condition, mechanical performance, and porosity. As shown in Figure 4, the as-built samples were sectioned along the build direction (Z-axis) using wire electrical discharge machining (W-EDM; HB600, Suzhou SanGuang, China) to facilitate assessment of the AM process's influence on porosity distribution. Generally, surface analysis reveals a typically rough morphology, which is critical, as it influences post-processing requirements and potential fatigue behavior.[45] Even if the bulk material has excellent mechanical properties, a rough surface can become a weak link. Therefore, enhancing fatigue life requires reducing Ra and improving overall surface integrity. Microhardness analysis was employed to evaluate the relative hardness distribution across the fabricated samples. Porosity analysis revealed the presence, shape, and distribution of residual pores, which are influenced by processing parameters such as *P*, *v*, and *h*. Effective monitoring and control of porosity (on the cross-section) are essential to ensure the structural integrity required for specific applications.

Table 3. Parameters used in the specimen production process (repeated over three runs with different build plate rotations)

Sample ID	Power (W)	Scan speed (mm/s)	Hatch spacing (µm)	Powder bed layer thickness (µm)	Volumetric energy density (J/mm³)
1	100	500	30	50	133.33
2	100	1,000	30	50	66.66
3	100	1,500	30	50	44.44
4	100	2,000	30	50	33.33
5	150	500	30	50	200
6	150	1,000	30	50	100
7	150	1,500	30	50	66.66
8	150	2,000	30	50	50
9	200	500	30	50	266.66
10	200	1,000	30	50	133.33
11	200	1,500	30	50	88.88
12	200	2,000	30	50	66.66
13	250	500	30	50	333.33
14	250	1,000	30	50	166.66
15	250	1,500	30	50	111.11
16	250	2,000	30	50	83.33
17	300	500	30	50	400
18	300	1,000	30	50	200
19	300	1,500	30	50	133.33
20	300	2,000	30	50	100

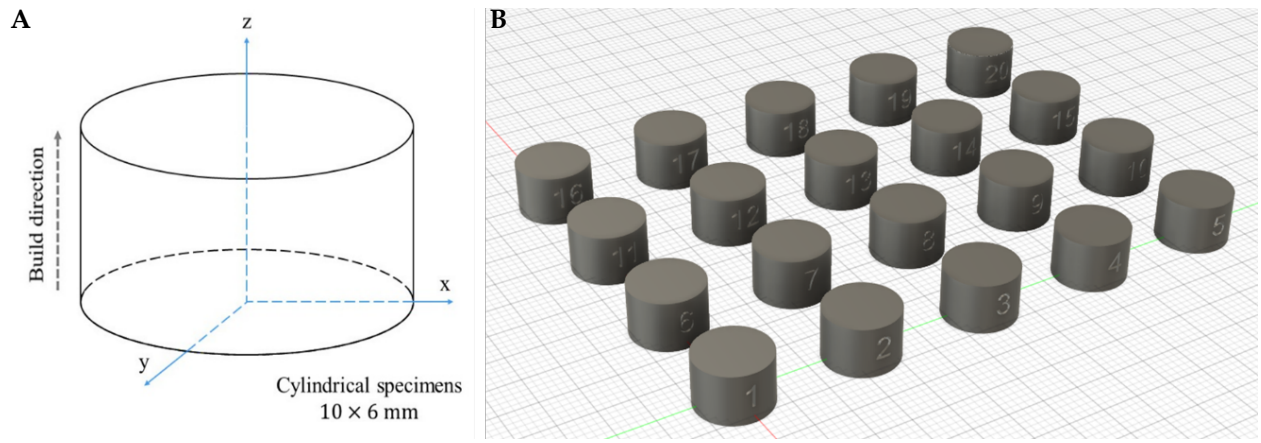

Figure 2. Design of specimen. (A) Schematic of the build direction and (B) computer-aided design model of the build job, including the 20 samples on the build plate with various parameters.

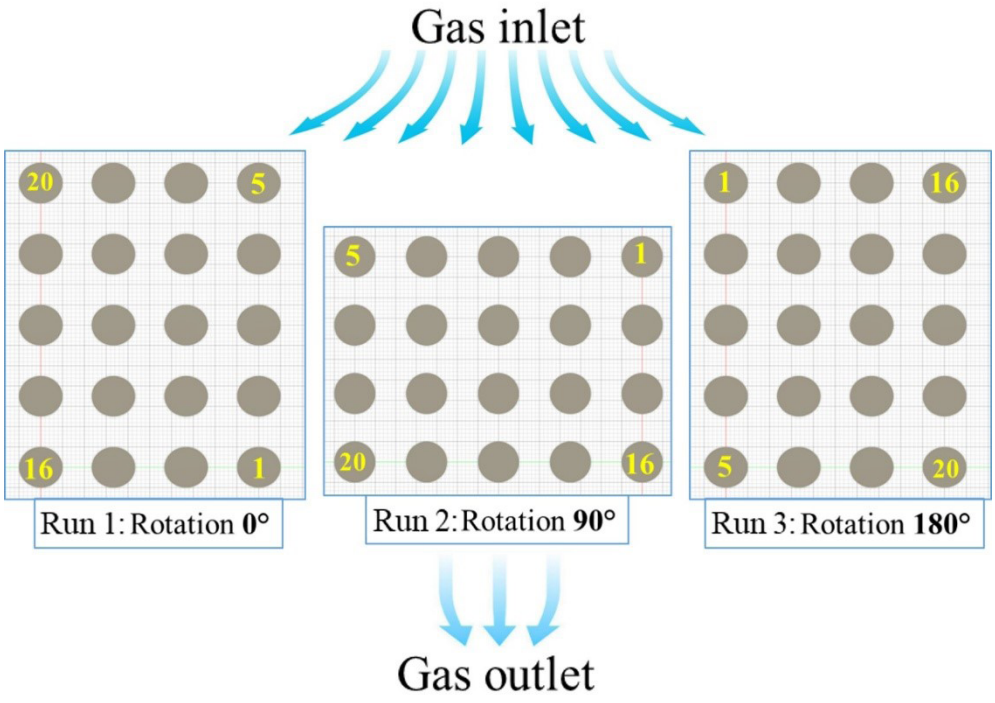

Figure 3. Various build-plate rotations (counter-clockwise) and changes in the specimen position relative to the gas flow inlet and outlet

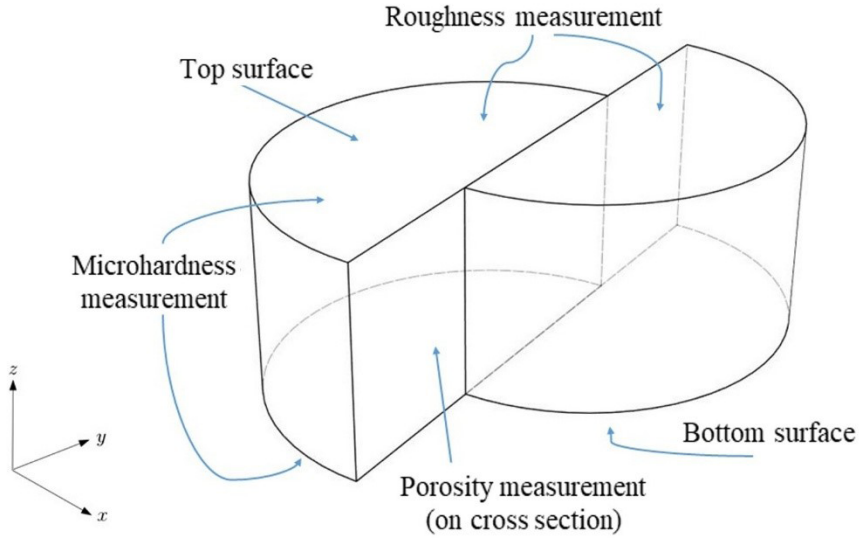

Figure 4. Scheme of the cylindrical sample processed by powder bed fusion–laser beam showing the locations of various analyses

2.2.1. Surface analysis

Due to rapid solidification and cooling, the nucleation rate exceeds the growth rate. Consequently, the fusion zone develops a fine, dense grain structure, which contributes to improved mechanical strength, as the Ra of 0.8 µm helps prevent premature failure from surface-initiated cracking.[46] However, Ra at the top of the melt pool can be influenced by a rippling phenomenon arising from surface tension-induced shear forces acting on the liquid metal. This effect is mainly driven by temperature variations between the area heated by the laser and the adjacent solidifying region, resulting from the movement of the laser. As these thermal gradients decrease, the opposing effects of gravity and the curvature of the melt pool surface work to restore the molten surface to its original level.[47] Nevertheless, due to the viscosity of the molten metal, this recovery process

is slowed, and the rapid solidification of the melt pool often prevents full surface leveling. In this study, the average Ra of the as-built specimens was analyzed using a 3D optical profilometer, the Sensofar S Neox (Sensofar Metrology, Spain), across all three runs. Measurements for each run were conducted in accordance with the ASME B46.1 2019 standard.[48]

2.2.2. Microhardness analysis

Nickel-based superalloys produced by PBF–LB have demonstrated mechanical properties comparable to or superior to conventionally manufactured materials (cast or forged) in hardness, tensile strength, and ultimate strength, but often exhibit low ductility.[49,50] The mechanical properties, especially the microhardness, of as-built IN625 alloy typically depend strongly on the building orientation. The specimens were cut from the build plate using W-EDM. Both surfaces (top and bottom) were then prepared using abrasive papers (grits 600, 800, 1,000, and 1,200) to obtain improved results. Subsequently, the microhardness was measured using the Vickers hardness test (UHL–VHMT–001, UHL, Germany) with a diamond indenter at a vertex angle of 136°, according to ISO 6507-1, applying a load of 1,000 gf for 15 s. Measurements were taken from both the top and bottom polished surfaces of the cylindrical samples (per run), and the final hardness was determined as the average of three measurements per surface.

2.2.3. Porosity analysis

Porosity is a material discontinuity defined as a volumetric property of porous media, indicating the volumetric ratio of the void space (pores, fractures, and cracks) occupied within the unit volume of the porous medium.[51] Depending on the final application of the product, pores can either negatively or positively affect the mechanical properties of AM parts. For instance, components intended for high-stress environments should be fully dense to minimize the risk of failure. Conversely, some biomedical implants are intentionally designed with a certain degree of porosity to promote osseointegration with biological tissue.[52] Poulin *et al.*[24] produced up to 10% porosity in laser powder bed-fused IN625 samples by intentionally seeding pores by changing the laser v to study the influence of porosity on long fatigue crack propagation behavior. By increasing the v from 960 mm/s to 1,920 mm/s (960, 1,440, 1,680, and 1,920 mm/s), the intentionally seeded porosities increased from 0.1% to 2.7% (0.1, 0.3, 0.9, and 2.7%). In this study, the P was presumably very low, which may have accounted for these results. Therefore, the relationship between v and porosity is not linear, and porosity increases when the v exceeds a threshold. Nevertheless, Ziegelmeier *et al.*[53] reported that the surface quality and porosity of the fabricated part were highly dependent on the packing density and roughness of the layered powder bed.

To prepare the samples for this part of the study, the cylindrical samples were cut perpendicularly via W-EDM, as this orientation (across the build direction) enables a more comprehensive porosity analysis (Figure 4). The metallographic preparation involved several steps: mounting with resin glass fiber black at 10 bar pressure for 5 min; grinding, which included both coarse and fine steps using progressively finer abrasive papers (600, 1,000, 1,200, and 1,400); and polishing, which was performed in stages using fine abrasives on polishing cloths. Finally, the polished samples were cleaned and prepared for porosity evaluation. The porosity was subsequently analyzed via a Keyence (Japan) VHX-700 digital microscope at 100× magnification and high resolution. The captured images were processed with ImageJ (version 1.54k), which detects and quantifies pores based on contrast differences between the material matrix and voids. The software calculates the total pore area within a given cross-section and divides it by the section's total area to determine the porosity percentage. This method provides a reliable and precise measurement of the closed porosity of additively manufactured components.

3. Results and discussion

3.1. Surface analysis

According to investigations, lower v and higher repetition rates can reduce top-surface roughness by stabilizing the melt pool and minimizing surface profile variations; however, they can significantly increase the melt pool volume and promote balling.[54-57] Figure 5, captured at 20× magnification with 2 × 2 stitching, illustrates variations in Ra associated with defect probabilities, such as keyholing (Figure 5A), balling (Figure 5B), LOF (Figure 5C), and dense regions (Figure 5D). These observations were made without any post-processing to evaluate the relationship between VED values and defect occurrence across all samples.

In accordance with the literature,[58-60] as shown in Figure 5A (VED: 400 J/mm^3) and Figure 5B (VED: 333 J/mm^3), keyhole pore formation can occur at high VED values. In addition, keyhole pores form at the end of the track when the laser is switched off or when melt flow instabilities are caused by oscillation.[61,62] Despite the reduction in VED, which can mitigate keyholing or balling, Figure 5C and 5D demonstrate that at low VED values of ~33 and 67 J/mm3, respectively, LOF defects and dense region defects are observed (Table 4). Furthermore, the numerical data were analyzed to extract more detailed insights. The R_a values for the three experimental runs (averaged values) are summarized in Table 4.

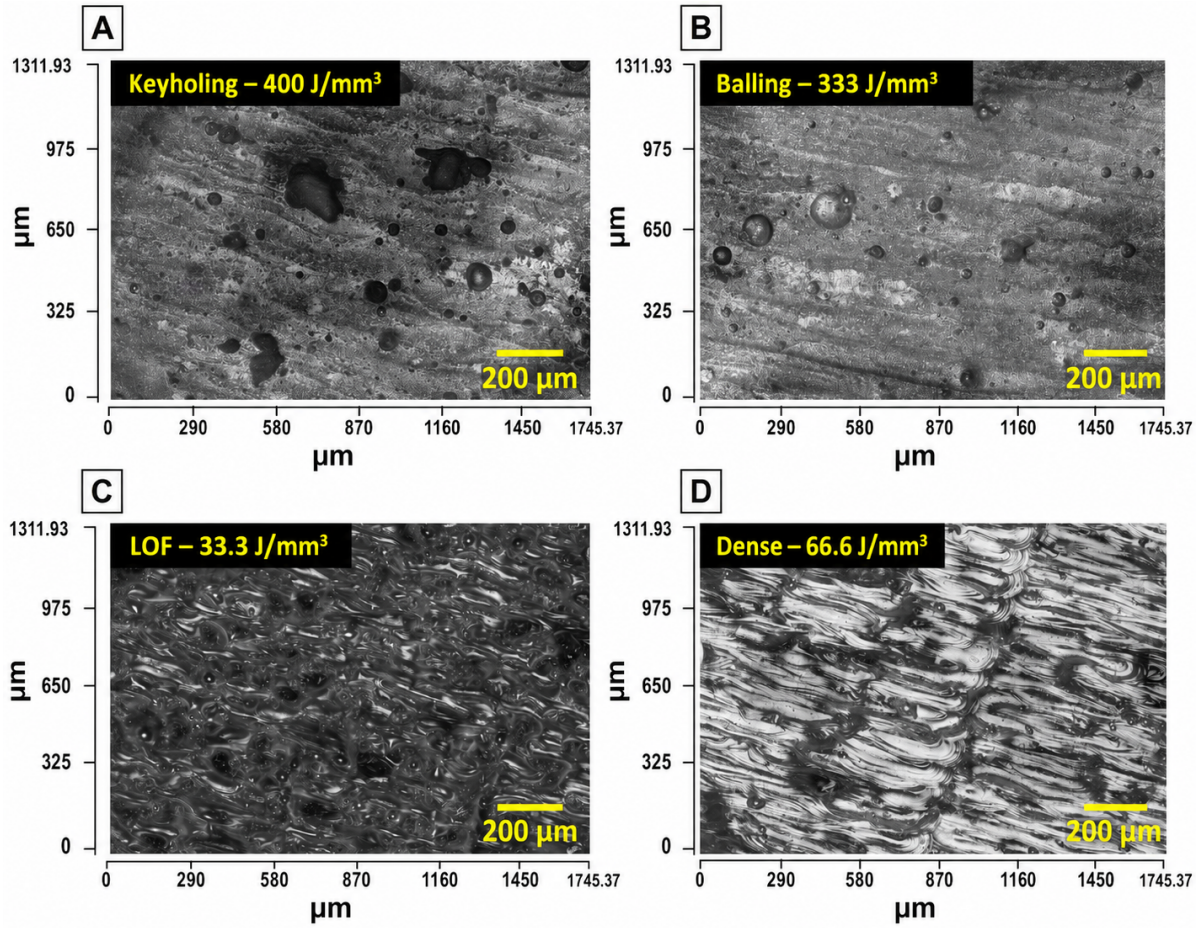

Figure 5. Surface morphology of the as-built parts produced by the powder bed fusion–laser beam method, as observed at 20× magnification with 2 × 2 stitching. (A) Image of sample No. 17, run 3. Keyholing defect. Volumetric energy density (VED): 400 J/mm³. (B) Image of sample No. 13, run 3. Balling defect. VED: 333 J/mm³. (C) Image of sample No. 04, run 3. Lack-of-fusion defect. VED: 33.3 J/mm³. (D) Image of sample No. 07, run 1. Dense region defect. VED: 66.6 J/mm³. Scale bar: 200 µm; magnification: 20×.

Based on a literature review, an approximate relationship between VED values and the types of defects (predicted defects) can be expressed as follows for IN625:

(i) VED ≤ 50 J/mm³: higher probability of LOF.
(ii) 50 J/mm³ < VED ≤ 100 J/mm³: dense regions with minimal defects.
(iii) 100 J/mm³ < VED <150 J/mm³: keyholing defects become more likely.
(iv) 150 J/mm³ < VED < 400 J/mm³: increased probability of keyholing and balling defects.

Although these defects have been identified and reported in other studies, they have been examined in greater detail in this work, with the findings presented in the "Real defect" column in Table 4. For instance, in samples No. 9, 13, and 17, *v* was constant and relatively low (500 mm/s), whereas *P* varied (200, 250, and 300 W). For the other samples, increasing *v* clearly increased Ra. Therefore, a lower *v* generally results in smoother surfaces, whereas a higher *v* generally results in increased roughness. In sample No. 1, despite the low *v*, the surface remains very rough because the *P* is very low (100 W). Thus, achieving a good surface finish on the as-built part requires not only an appropriate *v* but also a sufficient *P*. The balance between these two parameters is crucial for optimizing surface quality. Additionally, based on the images obtained from digital microscopy, an extra column has been added next to the predicted defects in Table 4 to illustrate the actual defects observed after processing each sample. In most cases, the predicted defects were accurate and are indicated by superscripted b ([b]). The samples with observed defects that did not match the predictions are indicated by superscripted c ([c]), while superscripted a ([a]) indicates additional defects that appeared in the as-built samples. Notably, balling was clearly observed in all the

samples, which may be attributed to the close spacing between them. The identified discrepancies between predicted and observed defects highlight the limitations of VED as a standalone predictive parameter.

Based on objective observations and analysis of the obtained images, in sample No. 1, although VED typically promotes keyholing defects, both *P* and *v* are low. This could explain why keyholing was not observed on the surface of the real samples. In sample No. 8, in addition to LOF, a dense region was observed. This could be due to the high *v* (2,000 mm/s), which may have prevented sufficient melt pool fluidity. In sample No. 11, in addition to the predicted defect, keyholing was observed exclusively during run 3, when the sample was positioned closest to the gas inlet in the first row exposed to the shielding gas. In contrast, all other samples in the same position exhibited only the predicted defect. This suggests that the orientation of the samples relative to the gas flow or build chamber geometry does not noticeably influence the surface texture under the tested conditions. Instead, Ra appears to be governed primarily by key printing parameters, particularly *v* and *P*. These parameters directly influence melt pool dynamics, solidification behavior, and the energy input per unit area, all of which play critical roles in determining the final surface quality of the printed parts.

Figure 6A shows the Ra value as a function of the laser *v* at various *P* levels used during sample production. At 100 W, the Ra values were generally high, indicating poor surface quality and a trend different from that in the

Table 4. Measurement of the roughness of the as-built samples related to the laser power and scan speed

Sample ID	Ra (μm)	SD	VED (J/mm³)	Predicted defect	Real defect
1	16.94	1.60	133	K	B[a]
2	11.33	1.08	67	D	D[b]/B[a]
3	13.69	1.47	44	LOF	LOF[b]/B[a]
4	16.77	0.55	33	LOF	LOF[b]/B[a]
5	9.33	4.05	200	K/B	K[b]/B[b]
6	10.98	2.00	100	D	D[b]/B[a]
7	10.80	1.74	67	D	D[b]/B[a]
8	10.84	0.47	50	LOF	LOF[b]/D[c]/B[a]
9	4.92	0.89	267	K/B	K[b]/B[b]
10	9.26	2.76	133	K	K[b]/B[a]
11	10.92	2.58	89	D	K[c]/D[b]/B[a]
12	11.52	1.43	67	D	D[b]/B[a]
13	5.63	1.33	333	K/B	K[b]/B[b]
14	7.04	0.71	167	K	K[b]/B[a]
15	13.02	4.06	111	K	K[b]/B[a]
16	10.66	0.01	83	D	D[b]/B[a]
17	6.24	0.72	400	K/B	K[b]/B[b]
18	8.46	1.33	200	K/B	K[b]/B[b]
19	15.99	3.94	133	K	K[b]/B[a]
20	16.73	3.95	100	D	D[b]/B[a]

Note: [a]Additional defects that appeared in the as-built samples; [b]Accurate predicted defects; [c]Observed effects that did not match predictions.
Abbreviations: B: Balling; D: Dense region; K: Keyholing; LOF: Lack-of-fusion; Ra: Surface roughness; SD: Standard deviation; VED: Volumetric energy density.

other cases. At 150 W, Ra improved slightly but remained relatively high. As v increased, the Ra value remained nearly constant, with little variation. The smoothest surface was observed at 200 W and 500 mm/s, corresponding to sample No. 9, and at this P, increasing v led to rougher surfaces. Additionally, at higher v values (>1,000 mm/s), the Ra values became almost the same as those observed at 150 W. For P values of 250 and 300 W, a similar trend was observed, with the smoothest surfaces occurring at a v of 1,000 mm/s. This indicates that v of approximately 1,000 mm/s, when combined with moderate to high P, is optimal for achieving improved surface quality. However, when P exceeded 100 W, and v increased to 1,500 mm/s, the Ra value increased.

In addition, regarding the VED and its influence on the surface quality of the manufactured samples, a clear trend was observed, as shown in Figure 6B. Higher VED values were associated with improved surface finish, as indicated by lower Ra, as shown by the green oval within the 267–400 J/mm^3 VED range. This improvement can be attributed to a more consistent energy input, which promotes stable melt pool formation and enhanced material consolidation. As the VED decreased, the surface of the final parts became noticeably rougher. This trend is illustrated by the red oval (VED 133–200 J/mm^3) and is even more pronounced in the orange oval (VED 50–100 J/mm^3). Consequently, lower VED values may lead to incomplete melting, unstable melt pools, and poor interlayer bonding, all of which contribute to increased surface irregularities.

In summary, this study confirms the validity of VED-based defect prediction models reported in the literature: keyhole and balling defects were observed in samples processed at VED > 150 J/mm^3, whereas LOF defects predominantly occurred at VED ≤ 50 J/mm^3. Dense regions with minimal porosity were typically found within the intermediate range (50–100 J/mm^3). From the Ra perspective, a lower v, combined with sufficient P, contributes to reduced surface irregularities. This behavior is attributed to a more stable melt pool and reduced thermal gradients, which minimize surface undulations and spattering. From a physical standpoint, this can be explained by the balance between energy input and heat dissipation. Stable melt pool conditions promote uniform solidification and reduce defect formation, while an excess or insufficient energy input leads to instability such as keyholing or LOF. Thus, the observed trends should be read in terms of melt pool dynamics rather than only the effect of VED.

Conversely, high v with low P led to increased roughness due to insufficient melting and instabilities in the melt pool. A strong inverse relationship was observed between VED and average Ra. Higher VED values result in smoother surfaces due to improved energy absorption, consistent melting, and enhanced inter-layer bonding. At lower VED values, incomplete melting, poor layer consolidation, and unstable melt flow significantly increase the Ra. These findings reinforce the importance of energy density optimization to improve the as-built surface finish. It should be noted that the present analysis is based on a simplified parameter framework in which hatch spacing and layer thickness were kept constant. This choice allows a simpler interpretation of VED-related trends; the interaction between these parameters and melt pool dynamics may further influence defect formation and material properties. This part of the analysis identified sample No. 9 (VED = 267 J/mm^3, P = 200 W, v = 500 mm/s; Figure 6) as exhibiting the best surface finish, with an Ra value of 4.92 μm, as shown in Table 4. This highlights the effectiveness of combining moderate-to-high P with moderate v for process stability and surface quality. Furthermore, while an increase in P generally improves the surface finish, it must be carefully balanced with the v to prevent keyholing or balling.

An unexpected but noteworthy observation is the consistent presence of balling across most samples, even in regimes not typically associated with this defect. This may be attributed to additional experimental conditions, such as sample proximity, powder packing density, or heat accumulation between neighboring tracks. This finding suggests that balling may not be solely governed by VED and warrants further investigation into mesoscale thermal interactions during PBF–LB processing.

3.2. Microhardness analysis

The microhardness results for all samples are illustrated in Figure 7A, sorted by VED value. According to Li *et al.*,[63] the as-built samples produced by the AM process had a greater hardness than the forged samples did (approximately 305 HV, indicated by the red dashed line) because of the finer microstructure typical of a PBF–LB/M material. The microhardness results revealed variability between the top and bottom surfaces of each sample. Notably, owing to the outlier HV values of samples 4 and 13 (<290 HV), they were excluded from this part of the analysis. However, both surfaces exhibited approximately the same hardness, with the top surface ranging from 290 HV to 312 HV and the bottom surface from 297 HV to 309 HV. However, some samples, such as 4 and 13, showed notably lower hardness values on the top surface, likely due to local defects, particularly in sample 4, caused by LOF defects, thermal gradients, or process-induced inconsistencies. In several cases (specimens 5, 10, 14, 15, and 18), the bottom surface exhibited significantly greater hardness than the top

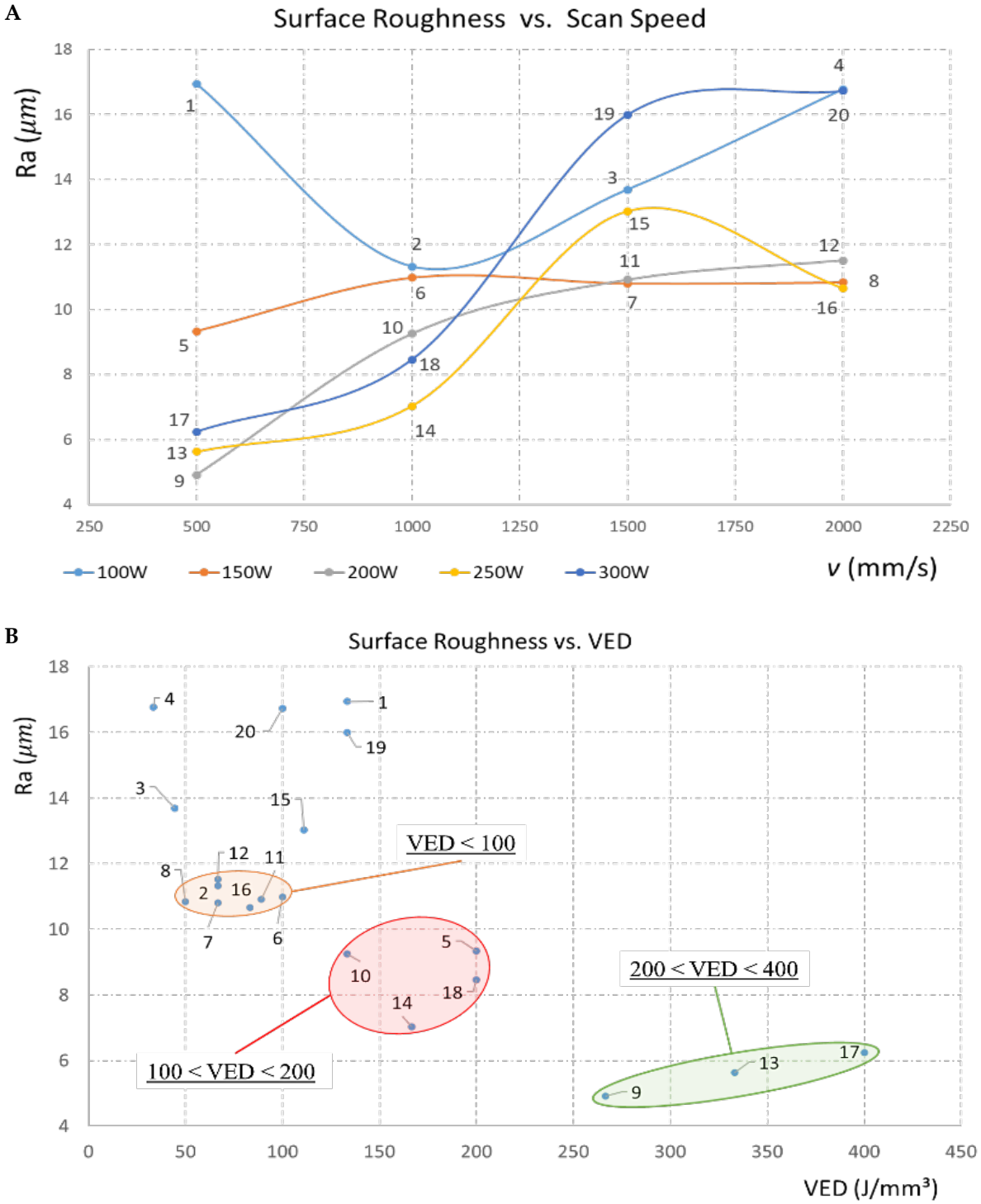

Figure 6. Surface roughness analysis. (A) Influence of the scanning speed and laser power on the average surface roughness. (B) Effect of volumetric energy density (VED) on average surface roughness.

surface, suggesting a higher relative VED in those regions (ranging from 111 to 400 J/mm^3), where keyholing and balling defects were identified. Additionally, factors such as cooling rates, heat accumulation in lower layers near the build plate, or localized phase transformations (e.g., white layer formation) may influence the material's hardness distribution.

Generally, the top layers are affected by rapid solidification, which can result in residual stresses or a heterogeneous microstructure, thereby reducing hardness consistency. In contrast, the bottom layers undergo repeated thermal cycling during deposition, which may induce grain refinement or secondary phase precipitation (e.g., δ-Ni3Nb or a Laves phase), thereby increasing hardness.[16]

On the other hand, when comparing microhardness across the different build plate orientations, most samples (with a few exceptions) show that run 1 yielded the lowest microhardness, whereas run 3 yielded the highest. These differences, however, are not relatively significant, with variations limited to approximately 12% on the top surface and up to 5% on the bottom surface, which can be compensated for by adjusting the processing parameters. As such, the effects of the rotation of the build plate and the position of the specimen on the microhardness can also be considered negligible.

Although higher VED values are generally associated with improved surface finish, as discussed in the previous section, an inverse relationship with hardness was observed. As illustrated in Figure 7, on the top surface, the samples with the highest VED values tended to exhibit lower microhardness values and vice versa. In contrast, on the bottom surface (except at the 250 W power level), an increase in the VED up to 200 J/mm^3 led to higher microhardness; the opposite trend was observed on the top surface. However, variations in microhardness between the top and bottom surfaces indicate a vertical temperature gradient, which is likely to affect microstructural evolution during processing. This behavior is likely driven by thermal cycling effects and prolonged heat exposure near the build plate, which promote grain refinement or precipitation hardening. Conversely, the top layers may experience more pronounced residual stress and incomplete melting due to rapid cooling and reduced reheating.

Regarding this issue, with respect to other parameters, such as P and v, the observed relationship between them can be attributed to the combined influence of energy input and the cooling rate, which could be evaluated as follows:

(i) At 100 W, increasing v significantly reduces HV values (approximately 13% on the top surface and approximately 9% on the bottom surface). This may be because increasing v reduces the energy input, leading to insufficient melting, weaker microstructures, and hence lower hardness.

(ii) In an opposite trend, at 250 W, increasing v resulted in an increase in HV values (around 11% on the top surface and nearly 5% on the bottom surface). This can be explained by the fact that a higher v at high P reduces excessive heat accumulation, promotes faster cooling, and leads to finer microstructures, thereby enhancing hardness.

(iii) At other P levels, the hardness remains relatively invariant to changes in v, indicating a threshold beyond which process stability is maintained.

Furthermore, samples 6, 8, 11, 16, and 19, with VED values ranging from 50–133 J/mm^3, exhibited the most uniform hardness across both surfaces, indicating well-balanced process parameters and minimal vertical thermal gradients. In contrast, anomalies in samples such as No. 4 (~33 J/mm^3) and No. 13 (~333 J/mm^3), both with HV values below 290 and considered outliers, showed significant differences between their top and bottom surfaces, which these discrepancies can be attributed to LOF or keyholing defects, as well as thermal inconsistencies during layer deposition.

3.3. Porosity analysis

For porosity analysis, cylindrical samples were cut perpendicularly using W-EDM across the build direction (Z-axis), enabling a more comprehensive analysis during production. Figure 8 shows the perpendicular surfaces of the samples at 100× magnification. This relatively high-magnification, high-resolution imaging technique was used to ensure high-quality, more accurate results.

The porosity measurement results shown in Figure 9 were averaged across three runs and 20 distinct samples, sorted by VED value. In this test, sample No. 4 was also considered an outlier, whereas the other samples were analyzed for two key parameters each. For each sample, two key parameters were evaluated: the mean % area, ranging from 0.024% to 0.454%, representing the area occupied by pores, and the mean pore count, ranging from 14 to 334. Despite variations in both parameters across the samples, the results indicate that the production settings were generally effective in achieving a dense material in most cases.

In this analysis, as shown in Figure 9 and considering the VED effect on porosity (% area and quantity), the lowest porosity quantity was observed in sample No. 15 (14 pores), with a VED value of 111 J/mm^3, and the lowest % area occupied by pores was recorded in sample No. 11 at 0.024%, corresponding to a VED value of 89 J/

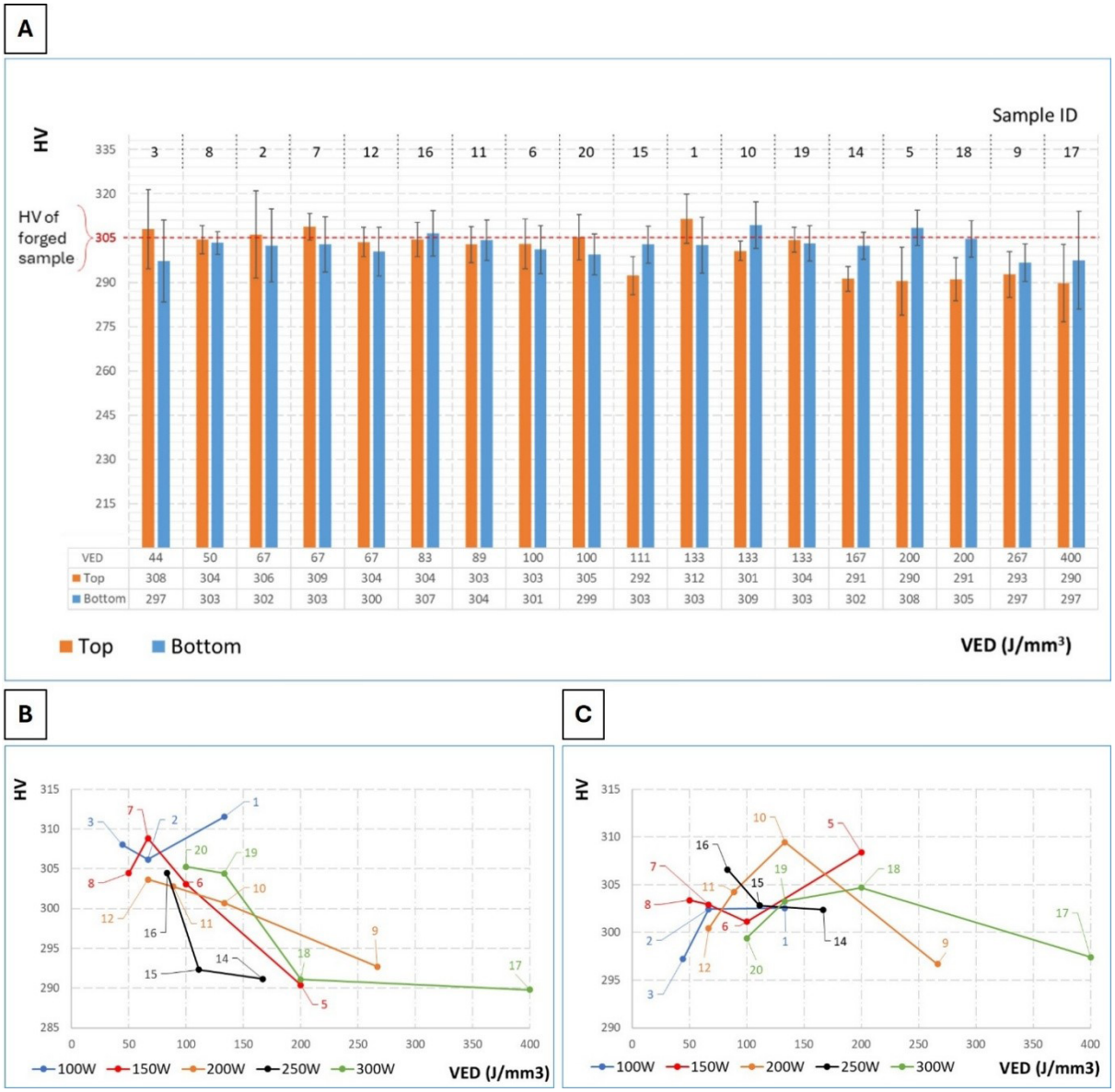

Figure 7. Microhardness analysis. (A) Microhardness comparison between powder bed fusion–laser beam as-built IN625 (Orange: Top surface and blue: bottom surface). The mean microhardness values as a function of laser power and volumetric energy density (VED) of (B) the top surface and (C) the bottom surface.

mm³. Several samples (e.g., Samples 2, 7, 10, 12, 14, 19, and 20) exhibited nearly zero pore quantity and a low area percentage, suggesting negligible porosity and a high-density material. Specimens 3, 5, 9, 13, and 17 had higher porosities (with 217–334 pores and 0.322–0.454% surface area occupied) or lower-than-average densities. These results suggest the presence of defects or inconsistencies such as LOF, keyholing, or balling in the material, which could be attributed to specific process parameters or conditions. More specifically, within the VED range of 50–167 J/mm³, the lowest porosity levels were observed in the as-built samples, with an average of up to 95 pores and an average porosity area of up to 0.25% (as indicated by the red dashed line).

In addition, the results indicated that a higher v, when combined with sufficient P, can enhance the material density while also improving the energy efficiency during manufacturing. Notably, at higher v, the reduced interaction time between the laser and the powder bed helps minimize overheating and mitigate defect mechanisms such as

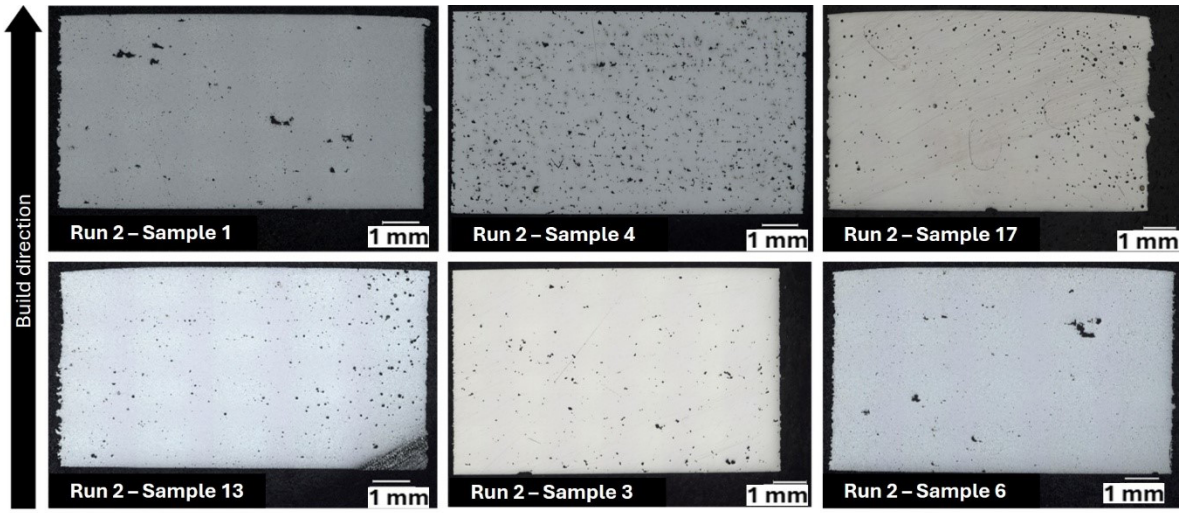

Figure 8. Perpendicular surface of the samples: Run 2. Scale bar: 1 mm; magnification: 100×.

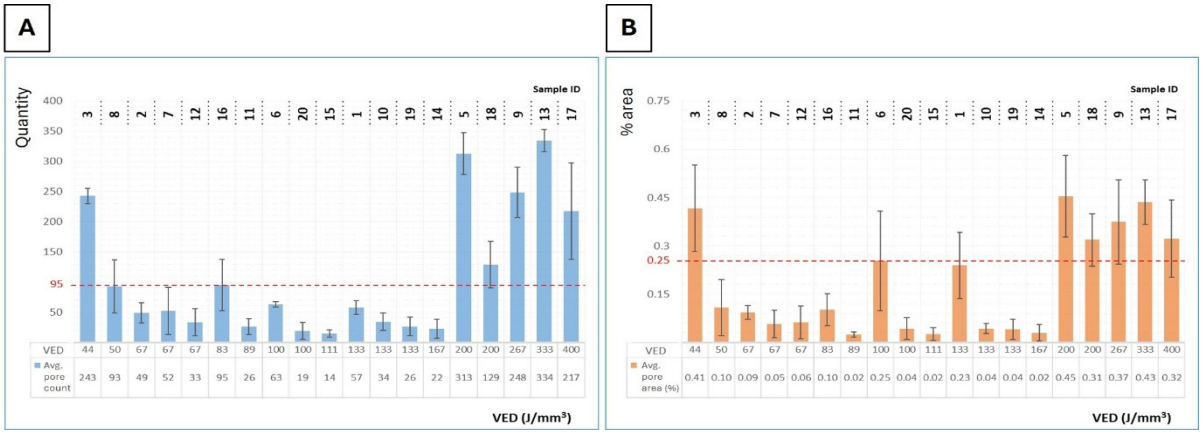

Figure 9. Relationship between volumetric energy density (VED) and average porosity characteristics of samples. (A) Average porosity quantity vs. VED. (B) Average % area porosity vs. VED.

keyholing and excessive melt pool instability. However, at the lowest *P* level (100 W), the energy input is likely insufficient to fully melt the powder at higher *v*, leading to incomplete fusion, higher porosity, and defects such as LOF and balling.[64] This highlights the importance of optimizing both *P* and *v* to achieve a suitable VED that ensures effective material consolidation without excessive energy use. Notably, no consistent pattern was observed across the various sample positions. Therefore, the effect of build plate rotation on material properties appears negligible for most samples and can be disregarded in this context. However, minor local variations may still occur due to other factors, such as localized thermal gradients or gas flow disturbances, which could warrant further investigation in more sensitive applications.

To quantify the relationship between pore count and the percentage of the total surface area they occupy, a metric called the porosity index was defined. This index was calculated as the ratio of the percentage of the total surface area occupied by pores to the total number of pores, as illustrated in Figure 10. The porosity index reflects the average relative size of individual pores within a material. Higher values indicate larger pores, whereas lower values indicate smaller, more uniformly distributed pores. For example, sample No. 1, with an index of 0.0042, has a large number of small pores, whereas sample No. 11, with an index of 0.0009, contains fewer but larger pores. Despite its simplicity, this metric offers a useful comparative measure for evaluating pore size distributions across different samples.

A

Sample ID	Avg. pore count	Avg. pore area (%)	Porosity index
1	57	0.239	0.0042
2	49	0.092	0.0019
3	243	0.417	0.0017
5	313	0.454	0.0015
6	63	0.253	0.0040
7	52	0.057	0.0011
8	93	0.108	0.0012
9	248	0.374	0.0015
10	34	0.042	0.0012
11	26	0.024	0.0009
12	33	0.062	0.0019
13	334	0.436	0.0013
14	22	0.029	0.0013
15	14	0.025	0.0018
16	95	0.101	0.0011
17	217	0.322	0.0015
18	129	0.318	0.0025
19	26	0.041	0.0016
20	19	0.043	0.0022

B

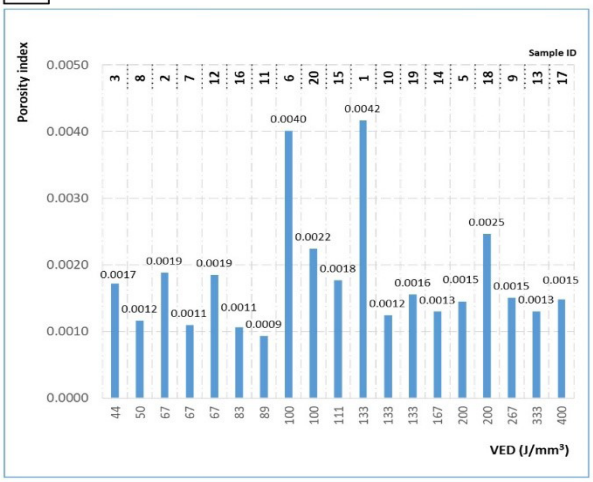

Figure 10. The relationship between the pore count and the percentage of area occupied expressed as the porosity index. (A) Average pore count and area (%). (B) Pore size ratio (quantity vs.% area).
Abbreviation: VED: Volumetric energy density.

In summary, porosity results vary significantly with processing parameters, as reported in the literature, which identifies incomplete fusion and melt pool instabilities as key contributors to elevated porosity. A non-monotonic relationship is observed between VED and porosity under the investigated parameter space. The samples with VED values between 50 and 167 J/mm^3 corresponded to optimal porosity levels, with an average porosity area of less than 0.25%. These findings indicate that within this intermediate VED range, the material density is maximized due to sufficient, but not excessive, energy input. At extremely low VED, LOF, and poor melt pool overlap dominate, while excessive VED may risk defects such as keyholing and increased energy consumption without necessarily improving porosity. Unlike many previous studies that focus on single output variables, this work provides a combined and experimentally validated analysis of Ra, porosity, and microhardness across the VED range, enabling a more comprehensive understanding of the process window. Additionally, a synergistic balance between P and v is essential for minimizing porosity while ensuring energy efficiency. Process parameters outside of the declared VED range, particularly low P with high v, result in incomplete melting and elevated defect levels. Conversely, while higher P and v combinations can achieve dense parts, they must be carefully controlled to avoid undesirable thermal effects and reduce energy inefficiency. However, the variations observed during the printing process can be primarily attributed to key process parameters, such as h, t, and especially v and P, which influence the VED value.

Regarding index porosity, no clear or consistent pattern has been observed to be established as a definitive result. Nevertheless, the relationship between pore quantity and pore size appears to be a critical factor. A greater number of small pores may lead to a more uniform distribution, whereas fewer but larger pores can create weak points in the material. This balance between pore size and distribution is particularly important, as it can significantly influence the occurrence of defects and, consequently, the overall quality, durability, and performance of the final AMed parts in their intended applications.

Overall, a key outcome of this study is the identification of a consistent process window in which surface quality, porosity, and microstructure are simultaneously optimized. This underlines the importance of considering multiple response variables rather than relying on a single metric. Similar VED values, obtained as an interaction of different parameter combinations, may lead to different material responses, reinforcing that the process–structure–property relationship in PBF–LB is governed by the interaction between parameters rather than only VED.

Based on the detailed analysis presented in this article, Table 5 has been created as a comprehensive guide summarizing the key relationships between process parameters, VED, and the resulting characteristics of IN625 fabricated by PBF-LB.

Table 5. Process parameter optimization guide for Inconel 625 using powder bed fusion–laser beam

VED (J/mm³)	*P* (W)	*v* (mm/s)	Defects	Porosity	R_a	HV	Comments
VED < 50	100–150	1,500–2,000	LOF (samples 3, 4, and 8)	High (~1.6%)	High (<13 μm)	271–290	Incomplete melting, high porosity - poor mechanical properties
60 < VED < 100	100–200	1,000–2,000	Dence regions (samples 2, 6, 7, 11, and 12)	Low (0.024–0.1%)	Moderate (10–12 μm)	299–309 (best hardness range)	Acceptable mechanical properties due to optimal balance between fusion and defect mitigation
110 < VED < 150	200–250	1,500–2,000	Keyholing onset (samples 1,10, 14, 15, and 19)	Low (slight increase)	Moderate to high (~13 μm)	291–312	Transition zone; careful tuning needed
160 < VED < 200	250–300	1,000–1,500	Keyholing/balling (samples 5, 14, and 18)	Moderate to high	Acceptable (~7–9 μm)	Drops slightly compared to the ideal range (due to overheating)	Best surface quality, but risk of internal defects from overheating
200 <VED < 400	250–300	500–1,000	Severe balling, keyholing (samples 4, 9, 13, and 17)	High (>1%)	Low (~ 6 μm) (very smooth surface)	~ 278–297	Overmelting - surface good - but internal quality and hardness may degrade

Abbreviations: HV: Vickers hardness; LOF: Lack-of-fusion; *P*: Power; Ra: Surface roughness; *v*: Scan speed; VED: Volumetric energy density.

4. Conclusion

In this study, IN625 samples were produced via PBF–LB technology under various process parameters, comprising 20 samples per run with different build plate rotations (Run 1: 0°, Run 2: 90°, and Run 3: 180°), and were thoroughly investigated. The results indicate a correlation between process parameter combinations (*v* and *P*) and the quality of the final product, with VED serving as a simplified descriptor. It was observed that both excessively high and low VED values can adversely affect the consolidation of powder layers. High VEDs led to defects such as keyhole porosity and balling, whereas low VEDs resulted in LOF due to insufficient energy input. Optimal combinations of *P* and *v* are essential for minimizing defects and achieving a dense and uniform microstructure.

In conclusion, for the successful fabrication of IN625 parts using PBF–LB, which is highly dependent on the precise optimization of process parameters, the following factors should be considered:

(i) An optimal process window corresponding to a VED range of 66–100 J/mm³ offers the best overall balance in terms of surface quality, porosity, and microhardness.

(ii) Extreme VED values should be avoided; values below 50 J/mm³ often lead to LOF defects and poor surface finish, while those above 167 J/mm³ increase the risk of keyholing and excessive thermal input.

(iii) A balanced relationship between *P* and *v* is crucial; lower *P* demands slower *v* to ensure proper melting, whereas higher *P* requires faster scanning to avoid overheating.

(iv) Additionally, the slight decrease in hardness observed at very high VEDs may be attributed to phase coarsening or residual thermal effects.

(v) Notably, the surface finish tends to improve with moderate to high VED levels, particularly when combined with low to medium *v*.

(vi) As a result, no consistent pattern was identified with respect to build plate orientation, and its overall influence can be considered negligible since the printing process is governed primarily by key parameters such as *h*, *t*, and especially *v* and *P*, which determine the VED value.

These findings underline the importance of precise parameter control in achieving high-quality PBF–LB-manufactured IN625 components.

Acknowledgments

None.

Funding

This study was conducted within the MICS (Made in Italy-Circular and Sustainable) Extended Partnership and received funding from the European Union NextGenerationEU (PIANO NAZIONALE DI RIPRESA E RESILIENZA (PNRR)\u2013MISSIONE 4 COMPONENTE 2, INVESTIMENTO 1.3\u2013D.D. 1551.11-10-2022, PE00000004). This manuscript reflects only the authors\u2019 views and opinions; neither the European Union nor the European Commission can be considered responsible for them.

Conflict of interest

Both Mariangela Quarto and Gianluca D'Urso serve as the Editorial Board Members of this journal, but were not in any way involved in the editorial and peer-review process conducted for this paper, directly or indirectly. All authors declare that they have no known competing financial interests or personal relationships that could have appeared to influence the work reported in this paper.

Author contributions

Conceptualization: Gianluca D'Urso, Sara Bocchi, Gabriele Locatelli
Formal analysis: Mohsen Afshani, Mariangela Quarto
Investigation: Mohsen Afshani, Gabriele Locatelli
Methodology: Mohsen Afshani, Tommaso Persico
Supervision: Gianluca D'Urso
Writing–original draft: Mohsen Afshani
Writing–review & editing: Gianluca D'Urso, Mariangela Quarto

Ethics approval and consent to participate

Not applicable.

Consent for publication

Not applicable.

Availability of data

The datasets used and/or analyzed during the current study are available from the corresponding author on reasonable request.

Further disclosure

This work has been previously deposited as a preprint on Research Square (doi: 10.21203/rs.3.rs-7760288/v1).

References

1. Li DC. Development of the Additive Manufacturing (3D printing) Technology. *Mach Build Autom*. 2013. Accessed April 25, 2026. https://en.cnki.com.cn/Article_en/CJFDTOTAL-ZZHD201304001.htm

2. Huang Y, Leu MC, Mazumder J, Donmez A. Additive manufacturing: Current state, future potential, gaps and needs, and recommendations. *J Manuf Sci Eng*. 2015;137(1):014001.

   doi: 10.1115/1.4028725

3. Chua CK, Leong KF, An J. Introduction to rapid prototyping of biomaterials. In: *Rapid Prototyping of Biomaterials*. Cambridge, UK: Woodhead Publishing; 2014:1-15.

   doi: 10.1533/9780857097217.1

4. Volpato GM, Tetzlaff U, Fredel MC. A comprehensive literature review on laser powder bed fusion of Inconel superalloys. *Addit Manuf*. 2022;55:102871.

   doi: 10.1016/j.addma.2022.102871

5. Rochus P, Plesseria JY, Van Elsen M, Kruth JP, Carrus R, Dormal T. New applications of rapid prototyping and rapid manufacturing (RP/RM) technologies for space instrumentation. *Acta Astronaut*. 2007;61(1-6):352-359.

   doi: 10.1016/J.ACTAASTRO.2007.01.004

6. Criales LE, Arısoy YM, Özel T. Sensitivity analysis of material and process parameters in finite element modeling of selective laser melting of Inconel 625. *Int J Adv Manuf Technol*. 2016;86(9):2653-2666.

   doi: 10.1007/S00170-015-8329-Y

7. Rashid R, Masood SH, Ruan D, Palanisamy S, Rahman Rashid RA, Brandt M. Effect of scan strategy on density and metallurgical properties of 17-4PH parts printed by Selective Laser Melting (SLM). *J Mater Process Technol*. 2017;249:502-511.

   doi: 10.1016/J.JMATPROTEC.2017.06.023

8. Liu Z, Wang Y, Wu B, Cui C, Guo Y, Yan C. A critical review of fused deposition modeling 3D printing technology in manufacturing polylactic acid parts. *Int J Adv Manuf Technol*. 2019;102(9):2877-2889.

   doi: 10.1007/S00170-019-03332-X

9. Sow MC, De Terris T, Castelnau O, *et al*. Influence of beam diameter on Laser Powder Bed Fusion (L-PBF) process. *Addit Manuf*. 2020;36:101532.

   doi: 10.1016/J.ADDMA.2020.101532

10. Ferro P, Meneghello R, Savio G, Berto F. A modified volumetric energy density–based approach for porosity assessment in additive manufacturing process design. *Int J Adv Manuf Technol*. 2020;110(7-8):1911-1921.

    doi: 10.1007/S00170-020-05949-9

11. Scipioni Bertoli U, Wolfer AJ, Matthews MJ, Delplanque JPR, Schoenung JM. On the limitations of Volumetric Energy Density as a design parameter for Selective Laser Melting. *Mater Des*. 2017;113:331-340.

    doi: 10.1016/J.MATDES.2016.10.037

12. Trevisan F, Calignano F, Lorusso M, *et al*. On the Selective Laser Melting (SLM) of the AlSi10Mg Alloy: Process, Microstructure, and Mechanical Properties. *Materials*. 2017;10(1):76.

    doi: 10.3390/MA10010076

13. Harun WSW, Manam NS, Kamariah MSIN, *et al*. A review of powdered additive manufacturing techniques for Ti-6al-4v biomedical applications. *Powder Technol*. 2018;331:74-97.

    doi: 10.1016/J.POWTEC.2018.03.010

14. Frazier WE. Metal additive manufacturing: A review. *J Mater Eng Perform*. 2014;23(6):1917-1928.

    doi: 10.1007/S11665-014-0958-Z

15. DebRoy T, Wei HL, Zuback JS, *et al*. Additive manufacturing of metallic components – Process, structure and properties. *Prog Mater Sci*. 2018;92:112-224.

    doi: 10.1016/J.PMATSCI.2017.10.001

16. Yonehara M, Ikeshoji TT, Nagahama T, *et al*. Parameter optimization of the high-power laser powder bed fusion process for H13 tool steel. *Int J Adv Manuf Technol*. 2020;110(1):427-437.

    doi: 10.1007/S00170-020-05879-6

17. Floreen S, Fuchs GE, Yang WJ. The Metallurgy of Alloy 625. In: *Superalloys 718, 625, 706 and Various Derivatives (1994)*. Warrendale, PA: TMS; 1994:13-37.

    doi: 10.7449/1994/SUPERALLOYS_1994_13_37

18. Shoemaker LE. Alloys 625 and 725: Trends in Properties and Applications. In: *Superalloys 718, 625, 706 and Various Derivatives (2005)*. Warrendale, PA: TMS; 2005:409-418.

    doi: 10.7449/2005/Superalloys_2005_409_418

19. Reed RC. *The Superalloys: Fundamentals and Applications*. Cambridge, UK: Cambridge University Press; 2006.

    doi: 10.1017/CBO9780511541285

20. Carter LN, Wang X, Read N, *et al*. Process optimisation of selective laser melting using energy density model for nickel based superalloys. *Mater Sci Technol*. 2016;32(7):657-661.

    doi: 10.1179/1743284715Y.0000000108

21. Marchese G, Garmendia Colera X, Calignano F, *et al*. Characterization and Comparison of Inconel 625 Processed by Selective Laser Melting and Laser Metal Deposition. *Adv Eng Mater*. 2017;19(3):1600635.

    doi: 10.1002/ADEM.201600635

22. Wang P, Zhang B, Tan CC, *et al*. Microstructural characteristics and mechanical properties of carbon nanotube reinforced Inconel 625 parts fabricated by selective laser melting. *Mater Des*. 2016;112:290-299.

    doi: 10.1016/J.MATDES.2016.09.080

23. Poulin JR, Kreitcberg A, Terriault P, Brailovski V. Fatigue strength prediction of laser powder bed fusion processed Inconel 625 specimens with intentionally-seeded porosity: Feasibility study. *Int J Fatigue*. 2020;132:105394.

    doi: 10.1016/J.IJFATIGUE.2019.105394

24. Poulin JR, Kreitcberg A, Terriault P, Brailovski V. Long fatigue crack propagation behavior of laser powder bed-fused inconel 625 with intentionally-seeded porosity. *Int J Fatigue*. 2019;127:144-156.

    doi: 10.1016/j.ijfatigue.2019.06.008

25. Koutiri I, Pessard E, Peyre P, Amlou O, De Terris T. Influence of SLM process parameters on the surface finish, porosity rate and fatigue behavior of as-built Inconel 625 parts. *J Mater Process Technol*. 2018;255:536-546.

    doi: 10.1016/J.JMATPROTEC.2017.12.043

26. Marchese G, Parizia S, Rashidi M, *et al*. The role of texturing and microstructure evolution on the tensile behavior of heat-treated Inconel 625 produced via laser powder bed fusion. *Mater Sci Eng A*. 2020;769:138500.

    doi: 10.1016/J.MSEA.2019.138500

27. Pleass C, Jothi S. Influence of powder characteristics and additive manufacturing process parameters on the microstructure and mechanical behaviour of Inconel 625 fabricated by Selective Laser Melting. *Addit Manuf*. 2018;24:419-431.

    doi: 10.1016/J.ADDMA.2018.09.023

28. Li C, Guo YB, Zhao JB. Interfacial phenomena and characteristics between the deposited material and substrate in selective laser melting Inconel 625. *J Mater Process Technol*. 2017;243:269-281.

    doi: 10.1016/J.JMATPROTEC.2016.12.033

29. Li C, White R, Fang XY, Weaver M, Guo YB. Microstructure evolution characteristics of Inconel 625 alloy from selective laser melting to heat treatment. *Mater Sci Eng A*. 2017;705:20-31.

    doi: 10.1016/J.MSEA.2017.08.058

30. Hu X, Zhao G, Liu F, Liu W. Microstructure and mechanical behavior of Inconel 625 alloy processed by selective laser melting at high temperature up to 1000 °C. *Rare Met*. 2020;39(10):1181-1189.

    doi: 10.1007/s12598-019-01321-3

31. Zhang J, Li S, Wei Q, Shi Y, Wang L, Guo L. Cracking behavior and inhibiting process of inconel 625 alloy formed by selective laser melting. *Chin J Rare Met*. 2015;39(11):961-966.

doi: 10.13373/J.CNKI.CJRM.2015.11.001

32. Zhang B, Bi G, Nai S, Sun CN, Wei J. Microhardness and microstructure evolution of TiB2 reinforced Inconel 625/TiB2 composite produced by selective laser melting. *Opt Laser Technol*. 2016;80:186-195.

doi: 10.1016/J.OPTLASTEC.2016.01.010

33. Gong H, Rafi K, Gu H, Starr T, Stucker B. Analysis of defect generation in Ti-6Al-4V parts made using powder bed fusion additive manufacturing processes. *Addit Manuf*. 2014;1-4:87-98.

doi: 10.1016/J.ADDMA.2014.08.002

34. Gong H, Rafi K, Gu H, Janaki Ram GD, Starr T, Stucker B. Influence of defects on mechanical properties of Ti-6Al-4V components produced by selective laser melting and electron beam melting. *Mater Des*. 2015;86:545-554.

doi: 10.1016/J.MATDES.2015.07.147

35. King WE, Barth HD, Castillo VM, *et al*. Observation of keyhole-mode laser melting in laser powder-bed fusion additive manufacturing. *J Mater Process Technol*. 2014;214(12):2915-2925.

doi: 10.1016/j.jmatprotec.2014.06.005

36. Tammas-Williams S, Zhao H, Léonard F, Derguti F, Todd I, Prangnell PB. XCT analysis of the influence of melt strategies on defect population in Ti-6Al-4V components manufactured by Selective Electron Beam Melting. *Mater Charact*. 2015;102:47-61.

doi: 10.1016/J.MATCHAR.2015.02.008

37. Zhou X, Wang D, Liu X, *et al*. 3D-imaging of selective laser melting defects in a Co-Cr-Mo alloy by synchrotron radiation micro-CT. *Acta Mater*. 2015;98:1-16.

doi: 10.1016/J.ACTAMAT.2015.07.014

38. Rai R, Burgardt P, Milewski JO, Lienert TJ, Debroy T. Heat transfer and fluid flow during electron beam welding of 21Cr–6Ni–9Mn steel and Ti–6Al–4V alloy. *J Phys D Appl Phys*. 2009;42(2):025503.

doi: 10.1088/0022-3727/42/2/025503

39. Benoit MJ, Mazur M, Easton MA, Brandt M. Effect of alloy composition and laser powder bed fusion parameters on the defect formation and mechanical properties of Inconel 625. *Int J Adv Manuf Technol*. 2021;114(3-4):915-927.

doi: 10.1007/s00170-021-06957-z

40. Todaro CJ, Rashidi M, Liu RL, *et al*. Laser powder bed fusion of high-strength and corrosion-resistant Inconel alloy 725. *Mater Charact*. 2022;194:112454.

doi: 10.1016/j.matchar.2022.112454

41. Schwerz C, Schulz F, Natesan E, Nyborg L. Increasing productivity of laser powder bed fusion manufactured Hastelloy X through modification of process parameters. *J Manuf Process*. 2022;78:231-241.

doi: 10.1016/J.JMAPRO.2022.04.013

42. Xu J, Wu Z, Niu J, *et al*. Effect of Laser Energy Density on the Microstructure and Microhardness of Inconel 718 Alloy Fabricated by Selective Laser Melting. *Crystals*. 2022;12(9).

doi: 10.3390/CRYST12091243

43. Everton SK, Hirsch M, Stavroulakis PI, Leach RK, Clare AT. Review of in-situ process monitoring and in-situ metrology for metal additive manufacturing. *Mater Des*. 2016;95:431-445.

doi: 10.1016/J.MATDES.2016.01.099

44. Yadroitsev I, Smurov I. Selective laser melting technology: From the single laser melted track stability to 3D parts of complex shape. *Phys Procedia*. 2010;5:551-560.

doi: 10.1016/J.PHPRO.2010.08.083

45. Hamidi Nasab M, Giussani A, Gastaldi D, Tirelli V, Vedani M. Effect of Surface and Subsurface Defects on Fatigue Behavior of AlSi10Mg Alloy Processed by Laser Powder Bed Fusion (L-PBF). *Metals*. 2019;9(10):1063.

doi: 10.3390/met9101063

46. Yuan X, Qiu H, Zeng F, *et al*. Microstructural evolution and mechanical properties of Inconel 625 superalloy fabricated by pulsed microplasma rapid additive manufacturing. *J Manuf Process*. 2022;77:63-74.

doi: 10.1016/J.JMAPRO.2022.03.008

47. Ramos JA, Bourell DL, Beaman JJ. Surface over-melt during laser polishing of indirect-SLS metal parts. *MRS Proc*. 2003;758:53-61.

doi: 10.1557/PROC-758-LL1.9

48. Kelechava B. ASME B46.1-2019: Surface Texture (Roughness, Waviness, Lay). *The ANSI Blog*. 2020. Accessed April 15, 2026. https://blog.ansi.org/ansi/asme-b46-1-2019-surface-texture-roughness-waviness/

49. Amato KN, Gaytan SM, Murr LE, *et al*. Microstructures and mechanical behavior of Inconel 718 fabricated by selective laser melting. *Acta Mater*. 2012;60(5):2229-2239.

doi: 10.1016/J.ACTAMAT.2011.12.032

50. Wang Z, Guan K, Gao M, Li X, Chen X, Zeng X. The microstructure and mechanical properties of deposited-IN718 by selective laser melting. *J Alloys Compd*. 2012;513:518-523.

doi: 10.1016/J.JALLCOM.2011.10.107

51. Lee KS, Kwon TH, Park T, Jeong MS. *Theory and Practice in Microbial Enhanced Oil Recovery*. Cambridge, MA: Gulf Professional Publishing (Elsevier); 2020:16-108.

doi: 10.1016/C2019-0-00983-1

52. Slotwinski JA, Garboczi EJ. Porosity of additive manufacturing parts for process monitoring. *AIP Conf Proc*.

2014;1581(1):1197-1204.

doi: 10.1063/1.4864957

53. Ziegelmeier S, Christou P, Wöllecke F, *et al*. An experimental study into the effects of bulk and flow behaviour of laser sintering polymer powders on resulting part properties. *J Mater Process Technol*. 2015;215:239-250.

doi: 10.1016/J.JMATPROTEC.2014.07.029

54. Niu HJ, Chang ITH. Liquid phase sintering of M3/2 high speed steel by selective laser sintering. *Scr Mater*. 1998;39(1):67-72.

doi: 10.1016/S1359-6462(98)00126-2

55. Fischer P, Romano V, Weber HP, Karapatis NP, Boillat E, Glardon R. Sintering of commercially pure titanium powder with a Nd:YAG laser source. *Acta Mater*. 2003;51(6):1651-1662.

doi: 10.1016/S1359-6454(02)00567-0

56. Kruth JP, Froyen L, Van Vaerenbergh J, Mercelis P, Rombouts M, Lauwers B. Selective laser melting of iron-based powder. *J Mater Process Technol*. 2004;149(1-3):616-622.

doi: 10.1016/J.JMATPROTEC.2003.11.051

57. Morgan R, Sutcliffe CJ, O'Neill W. Density analysis of direct metal laser re-melted 316L stainless steel cubic primitives. *J Mater Sci*. 2004;39(4):1195-1205.

doi: 10.1023/B:JMSC.0000013875.62536.FA

58. Yeung H, Kim FH, Donmez MA, Neira J. Keyhole pores reduction in laser powder bed fusion additive manufacturing of nickel alloy 625. *Int J Mach Tools Manuf*. 2022;183:103957.

doi: 10.1016/J.IJMACHTOOLS.2022.103957

59. Martin AA, Calta NP, Khairallah SA, *et al*. Dynamics of pore formation during laser powder bed fusion additive manufacturing. *Nat Commun*. 2019;10(1):1987.

doi: 10.1038/s41467-019-10009-2

60. Cunningham R, Zhao C, Parab N, *et al*. Keyhole threshold and morphology in laser melting revealed by ultrahigh-speed x-ray imaging. *Science*. 2019;363(6429):849-852.

doi: 10.1126/SCIENCE.AAV4687

61. Hojjatzadeh SMH, Parab ND, Guo Q, *et al*. Direct observation of pore formation mechanisms during LPBF additive manufacturing process and high energy density laser welding. *Int J Mach Tools Manuf*. 2020;153:103555.

doi: 10.1016/J.IJMACHTOOLS.2020.103555

62. Guo Q, Qu M, Escano LI, *et al*. Revealing melt flow instabilities in laser powder bed fusion additive manufacturing of aluminum alloy via in-situ high-speed X-ray imaging. *Int J Mach Tools Manuf*. 2022;175:103861.

doi: 10.1016/j.ijmachtools.2022.103861

63. Li S, Wei Q, Shi Y, Chua CK, Zhu Z, Zhang D. Microstructure Characteristics of Inconel 625 Superalloy Manufactured by Selective Laser Melting. *J Mater Sci Technol*. 2015;31(9):946-952.

doi: 10.1016/J.JMST.2014.09.020

64. Aboulkhair NT, Everitt NM, Ashcroft I, Tuck C. Reducing porosity in AlSi10Mg parts processed by selective laser melting. *Addit Manuf*. 2014;1-4:77-86.

doi: 10.1016/J.ADDMA.2014.08.001